Thermally activated increase of the average grain size as the origin of resistivity enhancement in NbO$_2$ films grown by pulsed-laser deposition

Nazir Jaber [1,*] Johannes Feldl,[2,*] Julian Stoever [1] Klaus Irmscher,[1] Martin Albrecht,[1]
Manfred Ramsteiner [2] and Jutta Schwarzkopf [1,†]

[1]*Leibniz-Institut für Kristallzüchtung, Max-Born-Straße 2, 12489 Berlin, Germany*
[2]*Paul-Drude-Institut für Festkörperelektronik, Leibniz-Institut im Forschungsverbund Berlin e. V.,*
Hausvogteiplatz 5–7, 10117 Berlin, Germany

We investigated NbO$_2$ thin films grown by pulsed-laser deposition on Al$_2$O$_3$(0001) substrates. Increasing the growth temperature from 700 to 900 °C, a clear improvement of the structural quality and the interface abruptness has been observed for the epitaxial films, together with an increase in the average grain size from tens of nanometers to above 100 nm. For achieving high film resistivities, increasing the average grain size is found to be crucial. For a more detailed investigation of the carrier transport characteristics, Raman spectroscopy is demonstrated as a powerful tool. In the case of relatively large grain sizes, we reveal that the film resistivities directly correlate with the carrier concentration in the NbO$_2$ grains. The results obtained for comparatively small grain sizes can be explained by carrier transport via a percolation mechanism along metallic grain boundaries in accordance with a previously reported model.

I. INTRODUCTION

Materials exhibiting metal-insulator transitions (MITs) are currently widely studied because of their potential with regard to various electronic applications like electrical switches or memory devices [1–12]. Amongst these materials, NbO$_2$ is of particular interest because of its relatively high MIT temperature of 1080 K [13–17]. The pronounced resistivity change in NbO$_2$ is accompanied by a structural phase transition from a distorted rutile structure (space group $I41/a$ with lattice parameters $a = 13.70$ Å and $c = 5.99$ Å) at low temperature to a rutile structure (space group $P42/mnm$ with $a = 4.85$ Å and $c = 3.03$ Å) at high temperature (> 830 °C) [18,19]. In order to exploit the switching properties of materials with MIT for low power consumption memory devices, thin films with well-defined structural and electrical characteristics must be provided. In particular, to achieve sufficient densities in vertical three-dimensional architectures, thin layers are required with a high room-temperature resistivity in the range of several kΩ cm [20]. This prerequisite demands knowledge of the relationship between deposition parameters, and structural and electrical properties in thin films which could be different from those of bulk materials. But up to now, experimental studies on NbO$_2$ thin films are rather limited due to the difficulty in preparing high-quality NbO$_2$ thin films with large resistivities. This is, on the one hand, caused by the lack of lattice matched substrates. Furthermore, owing to the complexity of the Nb-O system, in which NbO$_2$ is not the most stable modification, knowledge of fundamental properties of NbO$_2$ thin films is rather limited yet, whereas bulk NbO$_2$ is well known [19]. Recently, Stoever *et al.* succeeded to synthesize films by pulsed-laser deposition (PLD) on MgF$_2$(001) substrates which exhibit a room-temperature resistivity of 1 kΩ cm [21]. In their approach to increase the resistivity of thin films, postgrowth thermal annealing at 880 °C in a reduced oxygen atmosphere has been reported as the crucial synthesis step. The annealing induced resistivity increase by two orders of magnitude has been explained by the accompanied enlargement of the average grain size in the thin films. In the as-grown films with comparatively small grains, the conductivity has been concluded to be dominated by a percolation mechanism along highly conductive grain boundaries. In order to achieve large grain sizes in a similar approach directly during growth, a substrate temperature around 900 °C would have to be chosen. However, MgF$_2$ substrates are not stable in this temperature range [22]. For Al$_2$O$_3$ substrates, in contrast, growth at temperatures around 900 °C is possible, most likely rendering unnecessary a postgrowth annealing process. As an alternative substrate Al$_2$O$_3$ (hexagonal symmetry with lattice parameters $a_H = 4.785$ Å and $c_H = 12.99$ Å) is thermally stable ($T_{Fusion} = 2050$ °C) and electrically insulating making it suitable for high temperature growth and electrical measurements of expitaxial films.

Here, we demonstrate the heteroepitaxial growth of NbO$_2$ thin films on Al$_2$O$_3$ substrates by PLD. Increasing the substrate temperature during growth results in improved structural and electrical properties as well as larger grain sizes. We utilized a Raman spectroscopic approach in order to verify that a change in the conduction mechanism as well as an increase in the carrier concentration are responsible for the

---

*These two authors contributed equally to this work.
†jutta.schwarzkopf@ikz-berlin.de

relation between average grain size and resistivity in the NbO_2 films.

II. EXPERIMENTAL DETAILS

The NbO_2 films were grown on single-crystalline $Al_2O_3(0001)$ substrates by PLD, using a Nb_2O_5 target under a reduced oxygen atmosphere. The target was prepared by a solid-state routine from Nb_2O_5 powder with 99.99% purity. The substrate was placed at a distance of 60 mm above the target. An excimer KrF laser ($\lambda = 248$ nm) was used with a repetition frequency of 5 Hz. The laser beam was focused on the surface of the target to a spot size of 0.045 cm^2 with an energy of 65 mJ/pulse (laser fluence of 1.44 J/cm^2). The background pressure was varied between 0.0001 and 0.09 mbar consisting of 99.9% Ar and 0.1% O_2 and was present during the whole growth process. The substrate temperature during growth was varied 700 °C and 900 °C. All samples were cooled down after film growth under the same conditions in vacuum (cooling rate of 3 K/min at a pressure below 10^{-5} mbar with the power being switched off at a temperature of 150 °C). The obtained NbO_2 films have been found to be stable under ambient conditions with no indications for changes or degradation observable in experimental results obtained during several months after PLD growth.

A Bruker D8 Discovery x-ray diffractometer (XRD) system with a four-axis goniometer and well-collimated and monochromatic Cu $K\alpha_1$ radiation was used for structural characterization of the deposited films. High-resolution 2θ-ω and rocking curves (ω scans) were performed to characterize the phase composition and the structural quality of the layers. The in-plane epitaxial relationship between the film and the substrate was established by x-ray Φ scans. Film thicknesses around 90 nm were deduced for all films from x-ray reflectivity measurements using the same XRD system. A Bruker atomic force microscope (AFM) operated in the peak-force-tapping mode was used to characterize the topography of the films. The average grain size (D_{AFM}) was determined by using the Gwyddion watershed masking and statistics tool [23]. The choice of this method is motivated by the fact that the same approach has been used in Ref. [21] which allows us to directly compare our growth-temperature dependent grain sizes with those obtained by postgrowth thermal annealing. Furthermore, the same AFM based procedure has also been used in several other works on related oxide films [24,25]. Most importantly, the values obtained by this procedure are related to lateral grain sizes which are relevant for the measured resistivities obtained by lateral transport experiments (see discussion below). The resistivity of the NbO_2 films was measured in the van der Pauw geometry by using a LakeShore Hall system with four probe heads. The current was set to values between 20 and 500 nA depending on the sample conductivity.

Raman spectroscopic measurements were performed in backscattering geometry with optical excitation at 473 nm (2.62 eV) by a solid-state laser. The incident laser light was focused by a microscope objective onto the sample surface. The backscattered light was collected by the same objective, spectrally dispersed by an 80-cm spectrograph and detected by a liquid-nitrogen-cooled charge-coupled device.
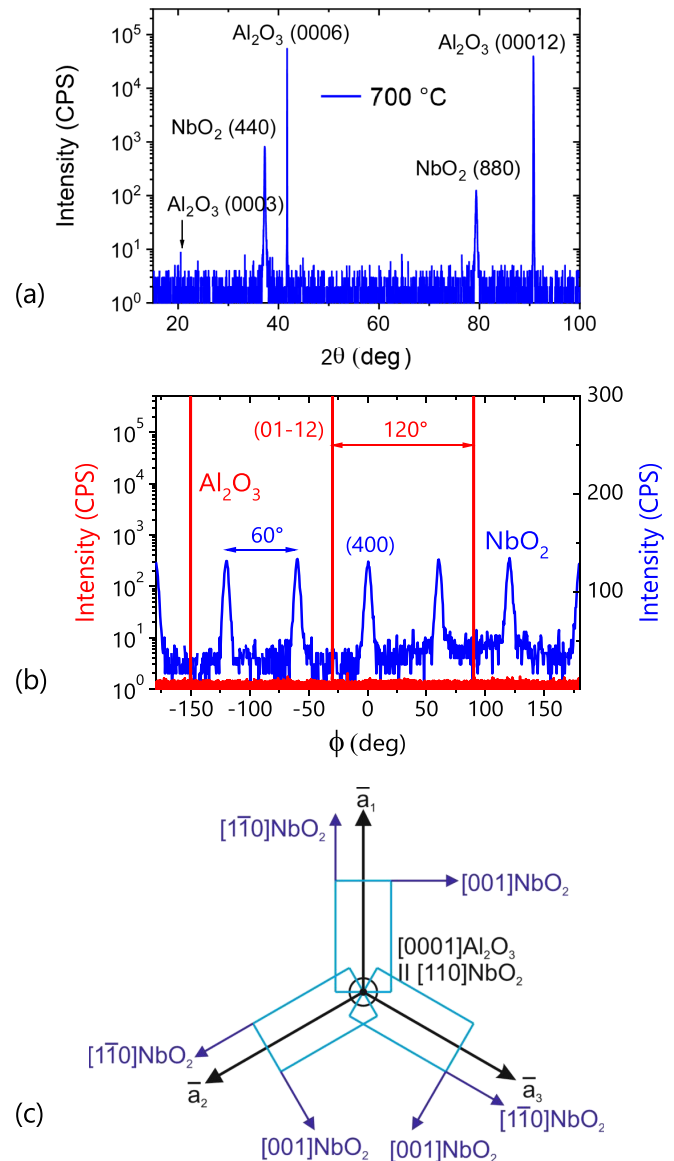

FIG. 1. (a) XRD 2θ-ω scan from a NbO_2 film deposited on a $Al_2O_3(0001)$ substrate at a growth temperature of 700 °C. (b) XRD in-plane Φ scans of the NbO_2 (400) reflection ($2\theta = 26°$ and $\chi = 45°$) (blue curve) and the Al_2O_3 (01$\bar{1}$2) reflection ($2\theta = 25.5°$ and $\chi = 57°$) (red curve). (c) In-plane arrangement of the NbO_2 unit cells (blue) with respect to the unit cell vectors of the hexagonal $Al_2O_3(0001)$ surface (black).

III. RESULTS AND DISCUSSION

A. Structural properties

Wide range out-of-plane 2θ-ω XRD scans of the samples under investigation exhibit only Bragg reflection peaks which either originate from the $Al_2O_3(0001)$ substrate or can be attributed to (110) oriented NbO_2. This finding is exemplarily shown in Fig. 1(a) for a sample grown at 700 °C with a background pressure of 0.03 mbar (S700.3 in Table I). The absence of any additional XRD peaks indicates the growth of single-phase NbO_2 with only (110) surface orientation. No foreign phase, especially Nb_2O_5, could be detected in accordance with the Raman spectroscopic results described

TABLE I. Resistivity ρ, substrate temperature during growth T_G, background pressure during growth P_G, NbO$_2$ film thickness d, grain size D, lattice parameter a, and the thickness of the depletion layer L_d normalized to the optical probing depth $\delta_{RS} = (2\alpha)^{-1} = 44$ nm.

Sample	ρ (Ω cm)	T_G (°C)	P_G (mbar)	d (nm)	D_{AFM} (nm)	a (Å)	L_d/δ_{RS}
S760.9	0.1	760	0.09	80	31	4.830	0.13
S700.3	2.3	700	0.03	91	35	4.831	0.14
S700.9	3.5	700	0.09	69	36	4.834	0.14
S760.3	9.5	760	0.03	80	48	4.834	0.17
S830.9	34.7	830	0.09	70	66	4.833	0.23
S830.3	40.1	830	0.03	84	89	4.837	0.25
S900.3	46.1	900	0.03	92	138	4.818	0.26
S900.0	165	900	0.0001	94	165	4.830	0.44

below. Figure 1(b) displays rotational Φ scans from the same sample for the (400) NbO$_2$ diffraction peak at $2\theta = 26°$ and $\chi = 45°$ (blue curve) and the $(01\bar{1}2)$ diffraction peak of the Al$_2$O$_3$ substrate at $2\theta = 25°$ and $\chi = 57.6°$ (red curve). The substrate scan exhibits three peaks equally separated by $120°$ due to the threefold symmetry of the Al$_2$O$_3$(0001) surface unit cell, while the ϕ scan of the NbO$_2$ thin film shows six peaks equally separated by $60°$. This result can be explained by the presence of rotational domains occurring with three different in-plane orientations of the tetragonal (110) NbO$_2$ unit cell, tilted by $120°$ with respect to each other [see Fig. 1(c)]. The corresponding epitaxial relationship between the NbO$_2$ film and the Al$_2$O$_3$ substrate is given by (110) NbO$_2$ $\parallel$ (0001) Al$_2$O$_3$ and $\langle 1\bar{1}0 \rangle$ NbO$_2$ $\parallel$ $\langle 10\bar{1}0 \rangle$ Al$_2$O$_3$, which is plausible due to the low lattice mismatch of -1.7% in $\langle 10\bar{1}0 \rangle$ directions of the Al$_2$O$_3$ substrate. The same kind of rotational domains have been found for films grown in the whole range of substrate temperatures between $700\,°$C and $900\,°$C.

The influence of the substrate temperature during growth on the structural film properties is demonstrated in Fig. 2 by the comparison of 2θ-ω and ω XRD scans of samples grown at the same background pressure of 0.03 mbar (samples S700.3, S830.3, and S900.3). The ω scans (rocking curves) around the (440) NbO$_2$ peak shown in Fig. 2(a) exhibit relatively narrow Bragg peaks superimposed on broad background features. While the full widths at half maximum (FWHM) of the narrow Bragg contributions [indicated by the arrows in Fig. 2(a)] are almost identical for the three samples (about $0.025°$), the rocking curves clearly differ in the relative contribution of the broad diffuse component. For the sample grown at the lowest temperature (S700.3), the two-component line shape is clearly evident and becomes less pronounced for the films grown at elevated temperatures. Such two-component diffraction patterns are often observed for heteroepitaxial thin films and can be explained by rotational disorder in the framework of a mosaicity model [26,27]. At the same time, the 2θ-ω scan of sample S900.3 [see Fig. 2(b)] exhibits pronounced thickness oscillations (Kiessig fringes) which cannot be seen for the films grown at lower temperatures. Both findings together, the occurrence of Kiessig fringes and the relatively weak contribution of the broad diffusive component in the rocking curve provide evidence for a superior structural and interface quality of the film grown at the highest temperature of $900\,°$C.

The evaluation of the peak positions in the 2θ-ω scans [see Fig. 2(b)] results in out-of-plane lattice parameters of the films (see Table I) which are well below the bulk lattice

parameter of unstrained NbO$_2$ (4.85 Å [17]). This decrease in the lattice parameters is attributed to residual tensile in-plane strain in the NbO$_2$ films, mainly due to the thermal mismatch between NbO$_2$ films (thermal expansion coefficient
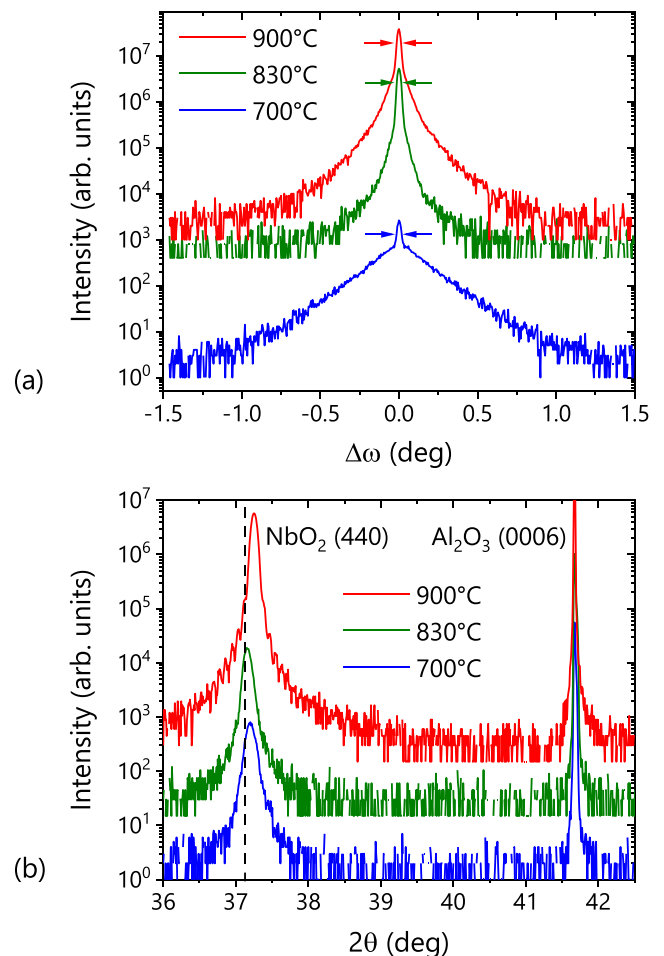

(a)

(b)

FIG. 2. (a) XRD ω scans around the (440) NbO$_2$ peak from NbO$_2$ films grown on Al$_2$O$_3$ at substrate temperatures of $700\,°$C (blue), $830\,°$C (green), and $900\,°$C (red). The arrows indicate the respective full widths at half maximum (FWHM). (b) XRD 2θ-ω scans for the same samples (S700.3, S830.3 and S900.3). The dashed vertical line corresponds to the peak position expected for unstrained NbO$_2$.
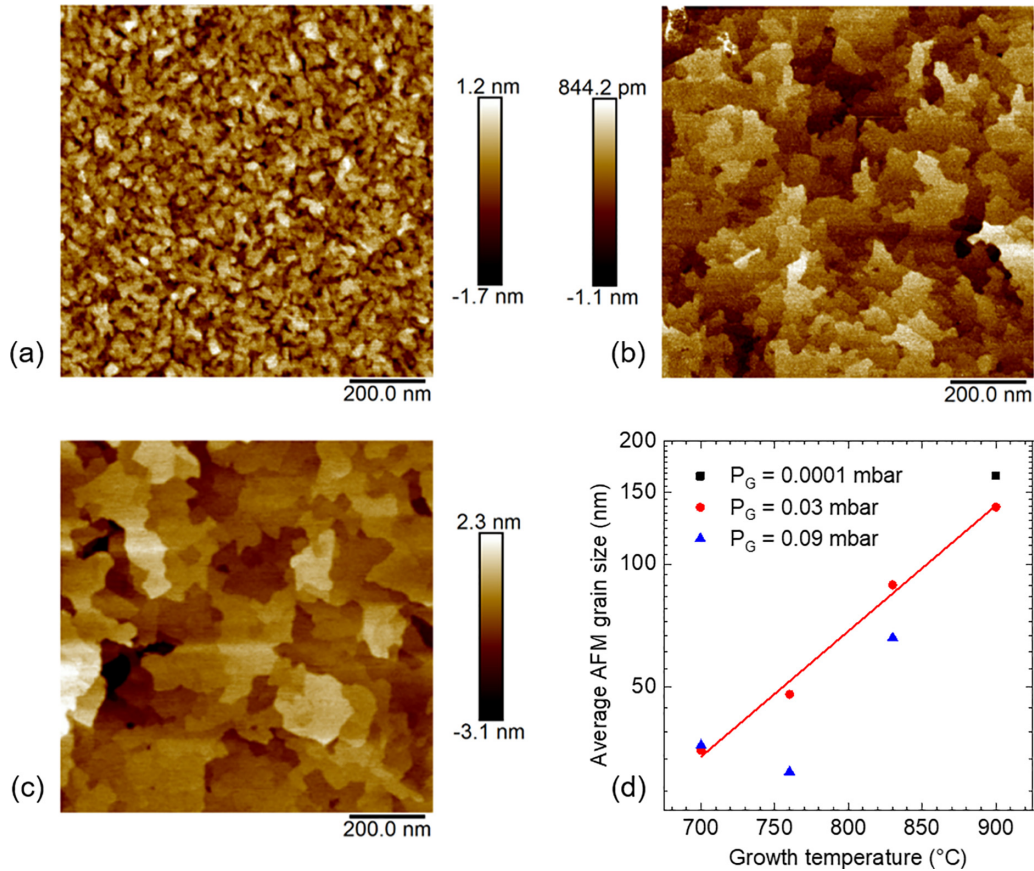
FIG. 3. AFM images of NbO_2 films grown on Al_2O_3 substrates at temperatures of (a) 700 °C, (b) 830 °C, and (c) 900 °C(samples S700.3, S830.3, and S900.3). The extracted average AFM grain size (D_{AFM}) as a function of the growth temperature is shown in (d) for films grown at different background pressures (P_G) as given in Table I. The solid red line is the result of a curve fitting for $P_G = 0.03$ mbar.

$\alpha_{film} = 4.8 \times 10^{-6}$ K^{-1}) [28] and Al_2O_3 substrate ($\alpha_{substr} = 8.1 \times 10^{-6}$ K^{-1}) [29].

The crucial dependence of the grain size on the growth temperature is shown in Figs. 3(a)–3(c) for NbO_2 films grown at the same pressure (here as an example at 0.03 mbar which corresponds to samples S700.3, S830.3, and S900.3). The surface morphologies imaged by AFM clearly unveil the existence of stacked grains and exhibit neither terraces resulting from a step-flow growth mode nor cracks or pinholes, even for scan areas of 10×10 μm^2 (not shown here). Most importantly, the AFM images reveal an enlargement of the average grain size with increasing growth temperature (cf. Table I). More generally, this correlation can be seen in Fig. 3(d) for all samples presented in Table I.

We cannot fully exclude a possible systematic uncertainty in the grain sizes D_{AFM} obtained from AFM images. However, the grain sizes D_{XRD} determined from the analysis of XRD data confirm the overall trend of an increasing grain size at elevated growth temperatures with absolute values of similar magnitude compared to those extracted from the AFM images. Thereby, the XRD grain sizes were calculated using Scherrer's formula $D_{XRD} = K\lambda/\beta\cos(\theta)$ where K (≈ 0.9) is the shape factor, λ the wavelength of the x-ray source (1.54065 Å for Cu $K\alpha$), β the FWHM of the Bragg peak (in radians), and θ the corresponding Bragg angle [30]. However, it has to be noted that for lateral grain sizes larger than the film thickness (d), the FWHM and D_{XRD} are determined by d. For

samples S900.3 and S900.0 (cf. Table I), for example, D_{XRD} has indeed been found to not exceed the respective film thickness. Furthermore, the FWHM β is also influenced by other factors such as the experimental resolution, microstrain, and defects. Therefore, the extracted D_{XRD} values represent only lower limits of the actual grain sizes. On the other hand, D_{AFM} is related to the lateral average grain size which is not limited by the film thickness (see Table I). In fact, similar lateral grain sizes have been obtained in Ref. [31] when comparing results extracted from AFM and transmission electron microscopy. Consequently, D_{AFM} is more relevant for the discussion of the electrical film characteristics since the resistivities discussed below have been determined by lateral transport measurements. A certain systematic deviation of the D_{AFM} values from the actual lateral grain sizes has no influence on the conclusions discussed below.

The observed increase of D_{AFM} [cf. Fig. 3(d)] is explained by the enhanced surface diffusion at higher substrate temperatures, which allows the adatoms to preferentially adhere at nucleated islands and results in the growth of larger grains. Additionally, we tentatively conclude from Fig. 3(d) that lower background pressures result in larger average grain sizes, which is assumed to be caused by the higher kinetic energy of the species in the plasma plume at lower pressure due to reduced scattering with the ambient gas particles. That means, enhanced surface diffusion and larger grain sizes can be obtained by both higher temperature and lower background

pressure. However, the impact of temperature is much larger and causes less defects in the films caused by the bombardment of the growing surface with high energetic plasma particles in gas of low background pressure. Note that the increase of the grain size from a few tens of nanometers at a growth temperature of $700\,°C$ to about 150 nm at a growth temperature of $900\,°C$ resembles the behavior which was obtained for NbO_2 films on MgF_2 as a consequence of postgrowth thermal annealing at $880\,°C$.

In summarizing the XRD and AFM data, it can be concluded that for higher substrate temperatures the desired larger average grain size and improved structural ordering are obtained at the same time. Due to the lower grain boundary density, the number of weakly bonded atoms at grain boundaries and the defect density are reduced which provide a lower stress relaxation. Since furthermore, the thermal expansion coefficient increases with decreasing grain size [32], higher substrate temperatures result in higher strain levels with lower defect density. All in all, NbO_2 films with the targeted structural characteristics can be synthesized at elevated temperatures on Al_2O_3 substrates without the need of postgrowth annealing.

B. Electrical characteristics

Resistivity measurements performed in the van der Pauw geometry reveal a significant enhancement of the resistivity (see Table I) with increasing growth temperature for the samples discussed above (S700.3, S830.3, and S900.3). This finding is consistent with the expected higher resistivity for films with larger average grain size [21]. However, the resistivity measurements alone do not provide further insight into the underlying reason for the observed behavior. Unfortunately, reliable Hall measurements of the free-carrier concentrations and mobilities were not possible for the present NbO_2 layers [21]. Therefore, we utilized Raman spectroscopy which has been demonstrated to be a powerful alternative tool to investigate the characteristics of free carriers in various materials [33]. Furthermore, a larger set of samples (see Table I) has been investigated in order to verify in a more reliable manner the relationship between the free-carrier characteristics and the average grain size in the NbO_2 films. With the exception of one sample (S760.9), the average grain size indeed increases monotonically with the growth temperature which confirms our expectation from the discussion above.

Room-temperature Raman spectra of the above studied NbO_2 films are shown in Fig. 4. All spectra are dominated by optical phonon lines at 156, 167, 332, 344, 393, and $402\ cm^{-1}$ [6,34,35]. In addition, weaker Raman phonon lines are observed at 143, 184, 215, 225, 249, 268, 562, 574, and $630\ cm^{-1}$ [34]. The spectra were found to be independent of the polarization configuration. Since Raman backscattering from the (110) surface of NbO_2 is expected to be strongly anisotropic [36], our finding confirms the above-mentioned mosaicity leading to a threefold in-plane symmetry for NbO_2 films on $Al_2O_3(0001)$ substrates. Since NbO_2 is a metastable niobium oxide phase, it is important to note that the Raman spectra shown in Fig. 4 do not exhibit any spectral signature of Nb_2O_5. In particular, the strong Raman line at $118\ cm^{-1}$ characteristic for Nb_2O_5 is absent in all spectra, indicating
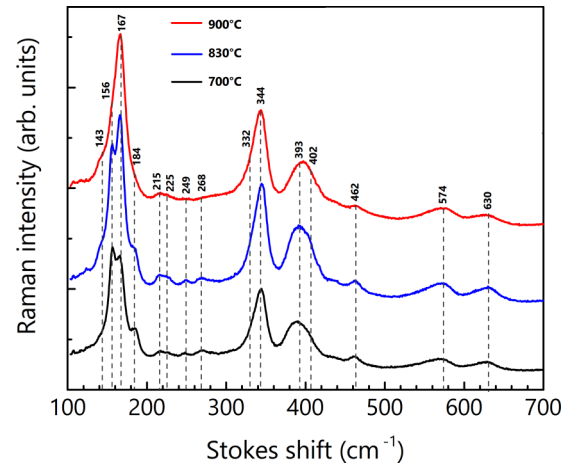

FIG. 4. Room-temperature Raman spectra of NbO_2 films grown on $Al_2O_3(0001)$ substrate for different substrate growth temperatures (samples S700.3, S830.3, and S900.3). For optical excitation a photon energy of 2.62 eV was used.

the existence of phase pure NbO_2 films in agreement with the above shown XRD results [37,38].

The Raman spectrum of NbO_2 comprises several pairs of transverse (TO) and longitudinal (LO) optical phonon modes [34]. Figure 5 displays one of these TO-LO phonon pairs in more detail for three different NbO_2 films. As can be clearly seen, the relative intensities of the TO and LO peaks around $160\ cm^{-1}$ depend on the growth temperature. The weaker peak around $180\ cm^{-1}$ is tentatively attributed to a so-called coupled LO-phonon plasmon (LPP) mode [39]. In polar semiconductors, the presence of free charge carriers leads to the coupling of LO phonons and plasmons via a macroscopic electric field [40–42]. The frequencies of the resulting coupled LPP modes are different from that of the uncoupled LO phonon mode and depend on the carrier density (n). This phenomenon can be utilized to investigate the free-carrier characteristics [33]. Most commonly, the carrier concentration is extracted from the peak positions of the LPP modes in Raman spectra. However, in solids with multiple TO-LO phonon pairs, such as NbO_2 [34], this kind of analysis is difficult due to the complex LPP coupling scheme (see, e.g., Refs. [43,44]). Furthermore, the LPP peak around $180\ cm^{-1}$ might be superimposed on (or even dominated by) a phonon peak reported in Ref. [45].

Another approach to gain information about the carrier density considers the fact that an uncoupled LO-phonon peak in Raman spectra originates exclusively from the space-charge layer at the surface which is depleted of free carriers. Since the corresponding scattering volume depends on the thickness of the space-charge layer (L_d), the intensity of the LO-phonon peak can be utilized as an inverse measure of the carrier density (see Ref. [46]):

$$I_{LO}(n) = I_0\{1 - \exp(-2\alpha L_d)\} \tag{1}$$

$$\text{with} \quad L_d = (2\epsilon\epsilon_0\phi/en)^{1/2}, \tag{2}$$

with α, ϵ, ϵ_0, and $e\phi$ being the optical absorption coefficient, the dielectric constant of NbO_2, the vacuum dielectric
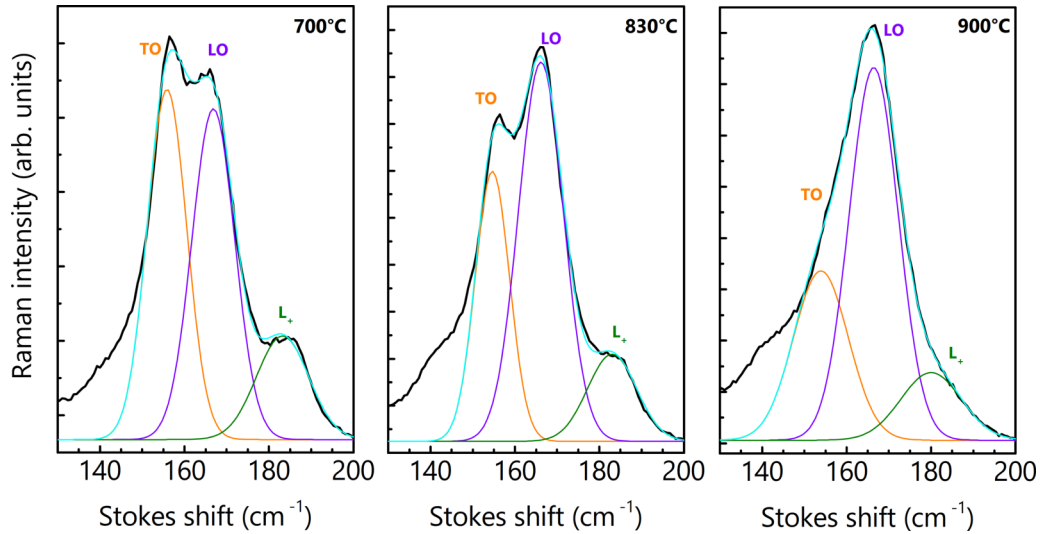
FIG. 5. Raman spectra of three NbO$_2$ films (samples S700.3, S830.3, and S900.3) in the frequency range of the TO-LO phonon pair at 160 cm^{-1} together with the simulations according to the fitting by Gaussian peak profiles.

constant, and the potential barrier height, respectively. Consequently, we attribute the different relative TO and LO intensities seen in Fig. 5 to a variation in the carrier density, as commonly observed for doped semiconductors [40,47]. Note, that the relative strong intensity of the LO-phonon peak is most likely caused by a Fröhlich-mechanism induced resonance enhancement [39,41].

In order to disentangle the relative influences of the carrier density (n) and mobility (μ) on the growth-temperature dependent variation of the resistivity, we consider two limiting cases using $n = \rho/e\mu$ in Eqs. (1) and (2):

$$I_{\text{LO}}(\rho) = I_0\{1 - \exp(-2\alpha c\rho^{1/2})\} \quad \text{for } \mu = \text{const}, \quad (3)$$

$$I_{\text{LO}}(\rho) = \text{const} \quad \text{for } n = \text{const} \quad (4)$$

with $c = (2\epsilon\epsilon_0\phi\mu)^{1/2}$. As a reasonable approximation, the absorption coefficient α can be assumed to be independent of the carrier density in our case since the photon energy used for optical excitation is far above the band gap of NbO$_2$.

For the analysis of the Raman data, the intensities of the superimposed TO and LO peak intensities at 155 and 165 cm^{-1} from all samples have been determined by Gaussian peak fittings. Thereby, the additional peak at 180 cm^{-1} has been included in the fitting procedure. Note that for other TO-LO phonon pairs (e.g., the one at 400 cm^{-1}), the deconvolution of the two peaks is more difficult making the extraction of the relative intensities unreliable. The corresponding spectra were excited with circularly polarized light in order to avoid any influence of polarization selection rules. Uncertainties in the LO peak intensities caused by variations in the optical alignment and the laser power were eliminated by using the TO peak intensity for normalization [47]. Scattering by TO phonons can be regarded to be not influenced by free carriers making the normalization justified under the condition that the optical probing depth ($1/2\alpha$) is smaller than the total film thickness. This prerequisite is clearly fulfilled for our samples (see Table I) since $1/2\alpha$ in NbO$_2$(110) is about 44 nm according to Ref. [36]. Furthermore, the spectra shown in Fig. 4

exhibit no spectral features from the Al$_2$O$_3$ substrate which provides evidence for the optical probing depth being smaller than the film thicknesses.

The normalized intensity $[I_{\text{LO}}(n)/I_{\text{TO}} = I^*_{\text{LO}}(n)]$ of the LO peak at 165 cm^{-1} is shown in Fig. 6 for all NbO$_2$ films as a function of the resistivity. For resistivities $\rho \geqslant 30$ Ω cm (average grain sizes $D_{\text{AFM}} \geqslant 60$ nm), the experimental data are well described by Eq. (3) assuming an Ohmic behavior with a constant carrier mobility. This finding shows that the assumption of a constant carrier mobility is a valid approximation for grain sizes $D_{\text{AFM}} \geqslant 60$ nm. The agreement with our model also reveals the existence of a surface depletion layer making the LO peak intensity an inverse measure of the carrier density. Consequently, the increase in resistivity for average
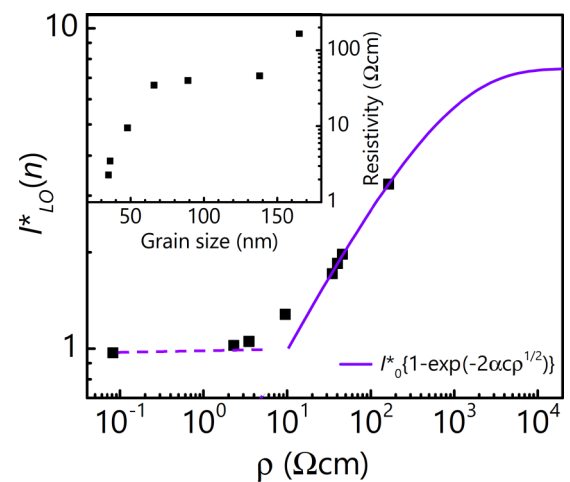

FIG. 6. Normalized LO-phonon peak intensity $I_{\text{LO}}(n)/I_{\text{TO}} = I^*_{\text{LO}}(n)$ as a function of the resistivity ρ for the NbO$_2$ films listed in Table I. The solid line is a fitting curve according to Eq. (3) using $(2\alpha)^{-1} = 44$ nm [36]. The obtained fitting parameters are $I^*_0 = 7.47$ and $c = 5.08 \times 10^{-7}$ cm/$\sqrt{\Omega}$. The dashed line corresponds to the case $n = \text{const}$ according to Eq. (4). The inset shows the resistivity ρ as a function of the average AFM grain size for the same samples.

grain sizes $D_{AFM} \geqslant 60$ nm is attributed to a decreasing carrier concentration in the semiconducting NbO_2 grains. Even the high resistivity of the sample with the exceptionally large average grain size (inset of Fig. 6) can be explained consistently by a particularly low carrier concentration described by the unique fitting curve according to Eq. (3). This reduction in the carrier concentration is most likely due to the improvement in structural quality with increasing growth temperature. For resistivities $\rho < 10\ \Omega$ cm (average grain sizes $D_{AFM} < 50$ nm), the nearly constant LO peak intensity indicates a saturation of the carrier density according to Eq. (4). The corresponding deviation from Eq. (3) for D_{AFM} below 60 nm can be explained by a qualitatively different carrier transport mechanism which is not related to the carrier concentration inside the NbO_2 grains. In fact, our observation is consistent with a percolation-type mechanism for which the conductivity is dominated by transport along metallic grain boundaries [21,48]. The pronounced decrease in the resistivity for grain sizes (D_{AFM}) below 60 nm can be clearly seen in the inset of Fig. 6. Altogether, our observations agree very well with the carrier transport model discussed in Ref. [21]. In this framework, it is also possible to confirm the validity of our Raman spectroscopic analysis. Even in the case of relatively small grain sizes, the only relevant carrier depletion region exists at the film surface since the grain boundaries are highly conductive. Furthermore, the optical probing depth is smaller than the film thickness for all samples (see Table I). Under this condition, also a possible depletion layer at the film/substrate interface does not have to be considered. Consequently, our analysis based on a surface depletion layer can be considered as a valid approximation.

Finally, it has to be mentioned that the maximum resistivity achieved for the NbO_2 films on Al_2O_3 substrates is still clearly below that observed for NbO_2 films on MgF_2 after postgrowth thermal annealing. Further studies and optimization of growth parameters is necessary to clarify whether or not resistivities in the kΩ cm range can also be reached for NbO_2 films on Al_2O_3 substrates without a postgrowth annealing step.

IV. SUMMARY AND CONCLUSION

PLD growth of NbO_2 on $Al_2O_3(0001)$ substrates enables the choice of sufficiently large substrate temperatures to synthesize thin films with average grain sizes above 100 nm without a postgrowth thermal annealing procedure. At the same time, the highest studied growth temperature of 900 °C leads to the best structural quality and abrupt interfaces. For the investigation of the carrier transport characteristics in NbO_2 films, Raman spectroscopy is shown to be a valuable tool. For average grain sizes above several tens of nanometers, the variation in the resistivity is shown to be caused by corresponding changes in the carrier concentration. For lower grain sizes, the observed behavior can be explained by a carrier transport based on a percolation mechanism along highly conductive grain boundaries in accordance with a previously reported model.

[1] M. Imada, A. Fujimori, and Y. Tokura, Rev. Mod. Phys. **70**, 1039 (1998).

[2] J. B. Torrance, P. Lacorre, A. I. Nazzal, E. J. Ansaldo, and C. Niedermayer, Phys. Rev. B **45**, 8209(R) (1992).

[3] F. J. Morin, Phys. Rev. Lett. **3**, 34 (1959).

[4] M. D. Pickett, G. Medeiros-Ribeiro, and R. S. Williams, Nat. Mater. **12**, 114 (2013).

[5] A. B. Posadas, A. O'Hara, S. Rangan, R. A. Bartynski, and A. A. Demkov, Appl. Phys. Lett. **104**, 092901 (2014).

[6] F. J. Wong, N. Hong, and S. Ramanathan, Phys. Rev. B **90**, 115135 (2014).

[7] K. Jung, Y. Kim, W. Jung, H. Im, B. Park, J. Hong, J. Lee, J. Park, and J.-K. Lee, Appl. Phys. Lett. **97**, 233509 (2010).

[8] J. Bae, I. Hwang, Y. Jeong, S.-O. Kang, S. Hong, J. Son, J. Choi, J. Kim, J. Park, M.-J. Seong, Q. Jia, and B. Ho Park, Appl. Phys. Lett. **100**, 062902 (2012).

[9] S. Spiga, A. Lamperti, C. Wiemer, M. Perego, E. Cianci, G. Tallarida, H. Lu, M. Alia, F. Volpe, and M. Fanciulli, Microelectron. Eng. **85**, 2414 (2008).

[10] X. Liu, S. M. Sadaf, S. Kim, K. P. Biju, X. Cao, M. Son, S. H. Choudhury, G.-Y. Jung, and H. Hwang, ECS Solid State Lett. **1**, Q35 (2012).

[11] J. Jeong, N. Aetukuri, T. Graf, T. D. Schladt, M. G. Samant, and S. S. P. Parkin, Science **339**, 1402 (2013).

[12] Z. Weibin, W. Weidong, W. Xueming, C. Xinlu, Y. Dawei, S. Changle, P. Liping, W. Yuying, and B. Li, Surf. Interface Anal. **45**, 1206 (2013).

[13] R. Janninck and D. Whitmore, J. Phys. Chem. Solids **27**, 1183 (1966).

[14] A. K. Cheetham and C. N. R. Rao, Acta Crystallogr., Sect. B: Struct. Sci., Cryst. Eng. Mater. **32**, 1579 (1976).

[15] R. Pynn, J. D. Axe, and R. Thomas, Phys. Rev. B **13**, 2965 (1976).

[16] K. Sakata, I. Nishida, M. Matsushima, and T. Sakata, J. Phys. Soc. Jpn. **27**, 506 (1969).

[17] A. A. Bolzan, C. Fong, B. J. Kennedy, and C. J. Howard, J. Solid State Chem. **113**, 9 (1994).

[18] A. O'Hara and A. A. Demkov, Phys. Rev. B **91**, 094305 (2015).

[19] C. Nico, T. Monteiro, and M. Graça, Prog. Mater. Sci. **80**, 1 (2016).

[20] S. K. Nandi, X. Liu, D. K. Venkatachalam, and R. G. Elliman, J. Phys. D: Appl. Phys. **48**, 195105 (2015).

[21] J. Stoever, J. E. Boschker, S. Bin Anooz, M. Schmidbauer, P. Petrik, J. Schwarzkopf, M. Albrecht, and K. Irmscher, Appl. Phys. Lett. **116**, 182103 (2020).

[22] K. Shibuya, J. Tsutsumi, T. Hasegawa, and A. Sawa, Appl. Phys. Lett. **103**, 021604 (2013).

[23] D. Nečas and P. Klapetek, Centr. Eur. J. Phys. **10**, 181 (2012).

[24] J. E. Boschker, T. Markurt, M. Albrecht, and J. Schwarzkopf, Nanomaterials **8**, 895 (2018).

[25] J. Martínez, E. Mosquera-Vargas, V. Fuenzalida, M. Flores, G. Bolaños, and J. Diosa, Nanomaterials **12**, 2578 (2022).

[26] P. F. Miceli and C. J. Palmstrøm, Phys. Rev. B **51**, 5506 (1995).

[27] P. F. Miceli, J. Weatherwax, T. Krentsel, and C. J. Palmstrøm, Phys. B: Condens. Matter **221**, 230 (1996).

[28] D. Music, A. M. Krause, and P. A. T. Olsson, Crystals **11**, 217 (2021).

[29] M. Halvarsson, V. Langer, and S. Vuorinen, Surf. Coat. Technol. **76-77**, 358 (1995).

[30] B. D. Cullity, *Elements of X-ray Diffraction* (Addison-Wesley, Reading MA, 1978).

[31] J. K. Dash, L. Chen, M. R. Topka, P. H. Dinolfo, L. H. Zhang, K. Kisslinger, T.-M. Lu, and G.-C. Wang, RSC Adv. **5**, 36129 (2015).

[32] R. Daniel, D. Holec, M. Bartosik, J. Keckes, and C. Mitterer, Acta Mater. **59**, 6631 (2011).

[33] G. Abstreiter, M. Cardona, and A. Pinczuk, in *Light Scattering in Solids IV*, edited by M. Cardona and G. Güntherodt (Springer, Berlin, Heidelberg, 1984) Vol. 54, pp. 5–150.

[34] F. Gervais, Phys. Rev. B **23**, 6580 (1981).

[35] Y. Wang, R. B. Comes, S. Kittiwatanakul, S. A. Wolf, and J. Lu, J. Vac. Sci. Technol. A **33**, 021516 (2015).

[36] A. O'Hara, T. N. Nunley, A. B. Posadas, S. Zollner, and A. A. Demkov, J. Appl. Phys. **116**, 213705 (2014).

[37] M. Palatnikov, O. Shcherbina, N. Sidorov, I. Skab, and K. Bormanis, Ukr. J. Phys. Opt. **13**, 207 (2012).

[38] I. Arsova, L. Arsov, N. Hebestreit, A. Anders, and W. Plieth, J. Solid State Electrochem. **11**, 209 (2006).

[39] D. Olego and M. Cardona, Phys. Rev. B **24**, 7217 (1981).

[40] H. Brugger, F. Schäffler, and G. Abstreiter, Phys. Rev. Lett. **52**, 141 (1984).

[41] A. Pinczuk and E. Burstein, Phys. Rev. Lett. **21**, 1073 (1968).

[42] H. Shen, F. H. Pollak, and R. N. Sacks, Appl. Phys. Lett. **47**, 891 (1985).

[43] M. Schubert, R. Korlacki, S. Knight, T. Hofmann, S. Schöche, V. Darakchieva, E. Janzén, B. Monemar, D. Gogova, Q.-T. Thieu, R. Togashi, H. Murakami, Y. Kumagai, K. Goto, A. Kuramata, S. Yamakoshi, and M. Higashiwaki, Phys. Rev. B **93**, 125209 (2016).

[44] A. Fiedler, M. Ramsteiner, Z. Galazka, and K. Irmscher, Appl. Phys. Lett. **117**, 152107 (2020).

[45] Y. Wang, Z. Nie, Y. Shi, Y. Wang, and F. Wang, Phys. Rev. Mater. **6**, 035005 (2022).

[46] R. Fukasawa, M. Wakaki, K. Ohta, and H. Okumura, Jpn. J. Appl. Phys. **25**, 652 (1986).

[47] A. Pinczuk, A. A. Ballman, R. E. Nahory, M. A. Pollack, and J. M. Worlock, J. Vac. Sci. Technol. **16**, 1168 (1979).

[48] V. Ambegaokar, B. Halperin, and J. Langer, J. Non.-Cryst. Solids **8-10**, 492 (1972).